

Optical Characterization of Oligo(phenylene–ethynylene) Self-Assembled Monolayers on Gold

Lee J. Richter,* Clayton S.-C. Yang, Philip T. Wilson,[†] Christina A. Hacker, and Roger D. van Zee

National Institute of Standards and Technology, 100 Bureau Drive, Gaithersburg, Maryland 20899-8372

Joshua J. Stapleton and David L. Allara

Department of Chemistry and The Materials Research Institute, The Pennsylvania State University, University Park, Pennsylvania 16802

Yuxing Yao and James M. Tour

Department of Chemistry and Center for Nanoscale Science and Technology, Rice University, Houston, Texas 77005

Received: February 19, 2004; In Final Form: June 4, 2004

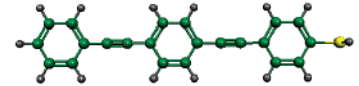
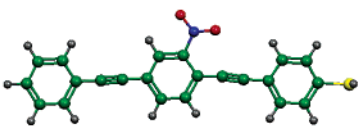
Vibrationally resonant sum-frequency generation (VR-SFG) and spectroscopic ellipsometry (SE) have been used to characterize self-assembled monolayer films of unsubstituted and mononitro-substituted oligo(phenylene–ethynylene) molecules on vapor-deposited Au substrates. When combined with quantum chemical calculations of the relevant transition moment directions, orientation distributions and electronic excitation spectra are obtained. The orientation distribution from VR-SFG is in good agreement with previous IR reflection studies, indicating both molecules are tilted from the surface normal by $\sim 30^\circ$. The calculated resonant hyperpolarizabilities are in good agreement with experimental spectra. The optical polarizability extracted from SE suggests strong intermolecular interactions, consistent with molecular exciton theory.

1. Introduction

Self-assembled monolayers (SAMs) of highly conjugated organic molecules have recently become subject to intense study.^{1,2} The interest in these films is driven in large part by attempts to understand their potential in molecule-based electronics;³ therefore, extensive characterization of their electrical properties,⁴ either in test devices,^{5,6} via scanned probe techniques,^{7–10} or via electrochemical techniques,¹¹ has been performed. Oligo(phenylene–ethynylene) compounds have emerged as a prototypical system, displaying a diversity of electrical behavior depending upon subtle changes in molecular structure. SAMs of 4,4'-di(phenylene–ethynylene)benzenethiol (OPE Table 1) on Au are perhaps the most well characterized.^{7,12–16} They exhibit significantly greater conduction vs alkanethiol films of comparable thickness.¹⁷ Depending on the details of the measurement, the I–V curve is asymmetric, indicating slight rectification.^{7,18} Substitution on the central ring results in dramatic changes in the electrical behavior.^{5,6} Specifically, films with a mononitro substitution (nitro-OPE, Table 1) have been reported to exhibit negative differential resistance (NDR) near room temperature.^{6,8,19}

Given the considerable interest in the electrical properties of oligo(phenylene–ethynylene)-derived films, it is notable that very little spectroscopic characterization exists in the literature. UV–vis spectroscopy and limited infrared reflection absorption spectroscopy (IRAS) have been reported on OPE,^{7,12} whereas

TABLE 1: Structures Used for Calculation of Vibrational Properties

OPE	
nitro-OPE	

a more extensive vibrational spectroscopy study has been reported on 4,4'-di(phenylene–ethynylene)-2'-ethyl-1-benzenethiol.²⁰ In a recent paper,²¹ IRAS, single wavelength ellipsometry, contact angle, X-ray photoemission spectroscopy (XPS), and atomic force microscopy (AFM) were applied to the study of SAMs of OPE and nitro-OPE. It was discovered that the composition of the nitro-OPE SAMs depends sensitively on the assembly procedure, and the nitro-OPE SAMs are significantly less stable than those of OPE. Under the best assembly and storage conditions, both SAMs were observed to be well-organized with an ordered lattice.

In this paper, vibrationally resonant sum-frequency generation (VR-SFG) and spectroscopic ellipsometry (SE) are applied to the study of OPE and nitro-OPE SAMs. Quantitative analysis of the polarization dependence of the VR-SFG spectra, combined with quantum chemical calculations of the hyperpolarizability tensor elements, provides insights into the orientation

* Corresponding author. E-mail: lee.richter@nist.gov.

[†] Current address: Milliken Research Corporation, 920 Milliken Road, Spartanburg, SC 29303.

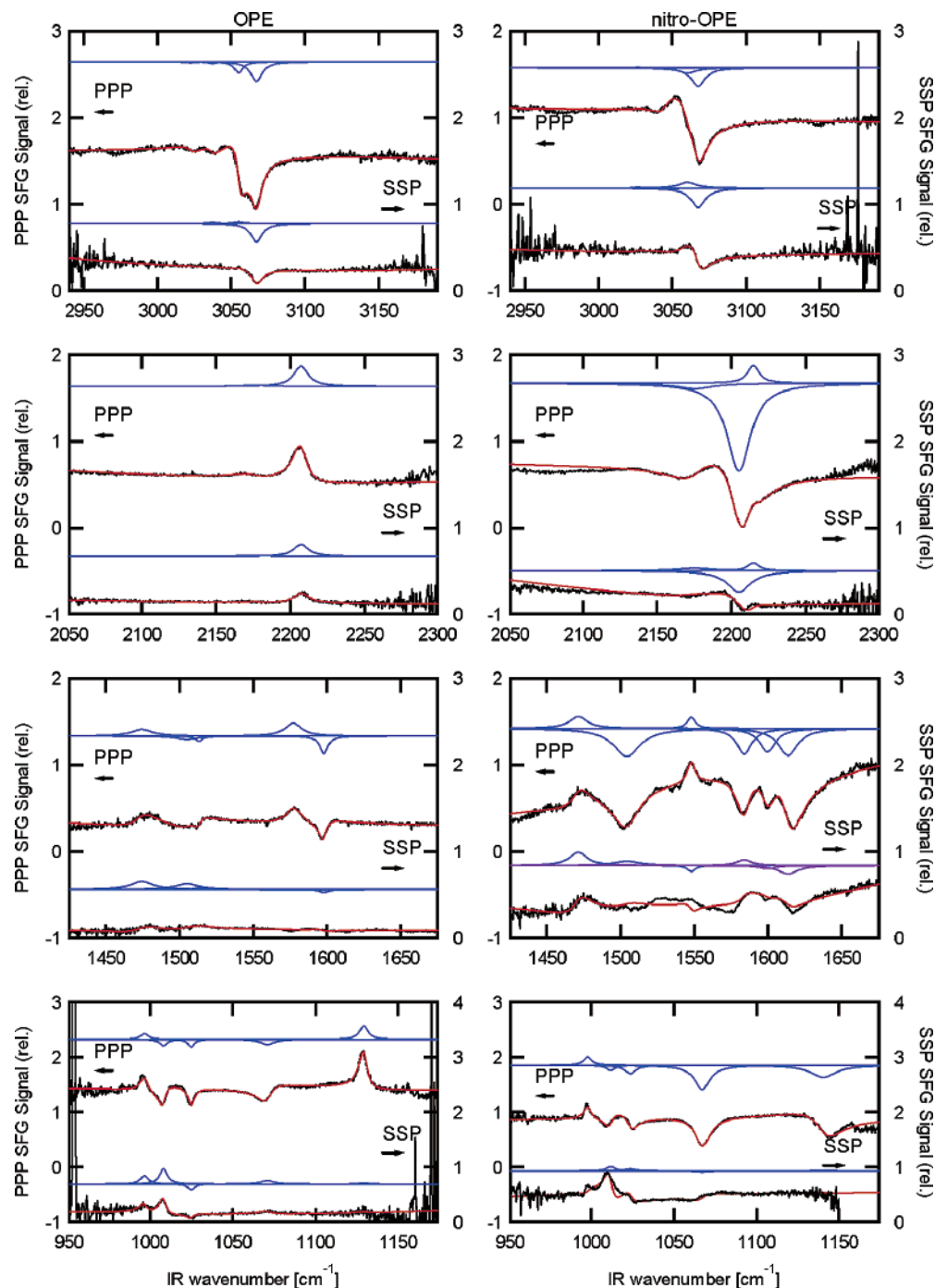


Figure 1. SFG spectra for OPE (left column) and nitro-OPE (right column). PPP spectra are plotted with respect to the left axis, SSP spectra with respect to the right axis. Also shown are fits (red: see text) to the data, and the imaginary part of the resonant components of the fits (blue: see text).

distribution of the adsorbed molecules. The optical transitions of the SAMs, reflected in the ellipsometric spectra, provide information on the coupling of electronic excitations in the films. The resulting thorough characterization provides both important ground-state information for the development of theories^{22–24} for the electrical behavior of this family of films and baseline spectra for future *in situ* studies of oligo(phenylene–ethynylene) chemistry.

2. Experimental Section

The synthesis of the molecules and the film preparation are as described in ref 21. Briefly, the substrates were ≈ 100 -nm-thick vapor-deposited Au films on Cr-primed Si wafers. They

were either used immediately or stored in laboratory ambient conditions and then cleaned via UV–ozone exposure. The solutions were $(0.1–0.5) \times 10^{-3}$ mol/dm³ in ethanol or 1:1 dichloromethane/ethanol. The OPE films were prepared from the thiol, and the nitro-OPE films were prepared from the thiol acetate using acid deprotection to eliminate the side reactions of the nitro group.^{15,21} Solution preparation and SAM formation was performed in a nitrogen-purged glovebox with the O₂ concentration kept below 2 ppm. The nitro-OPE compound has been reported to degrade upon exposure to laboratory ambient conditions.²¹ During the course of this work, significant evolution of the VR-SFG and SE spectra for the nitro-OPE were observed after only 4 days exposure to ambient conditions.

TABLE 2: SFG Vibrational Analysis for OPE

observed frequency (cm ⁻¹)	(A _r ^{ssp} /A _r ^{ppp})	assignment	calculated (a _r) (∂α/∂Q)(∂μ/∂Q)/(10 ⁻²³ C ² m V ⁻¹ kg ⁻¹)				
			z'z'z'	x'x'z'	y'y'z'	x'z'x'	y'z'y'
3068	0.30 ± 0.02	2 top	-3.8	-5.1	-0.4	0.0	0.0
3055	-0.01 ± 0.03	7a top	-8.4	1.1	0.0	0.0	0.0
2209	0.15 ± 0.01	C≡C sym	116	0.0	0.0	0.0	0.0
1598	0.06 ± 0.02	8a	-40	1.2	0.0	0.0	0.0
1576	-0.08 ± 0.09	8a	63	-1.8	0.0	0.0	0.0
1508	-0.29 ± 0.02	19a	-8.8	0.0	0.0	0.0	0.0
1474	0.37 ± 0.13	19a	4.8	0.0	0.0	0.0	0.0
1129	0.09 ± 0.09	9a	26	1.1	0.0	0.0	0.0
1070	-0.13 ± 0.04	18a bot + C-S	-5.3	-0.6	0.0	0.0	0.0
1024	0.16 ± 0.11	18a top	-1.3	-0.4	0.0	0.0	0.0
1009	-irr ^a	18a bot	-4.7	-0.3	0.0	0.0	0.0
996	-irr-	12 top	1.4	0.2	0.0	0.0	0.0

^a The A^{ssp}/A^{ppp} ratio was irreproducible over multiple determinations due to limited signal in the SSP configuration.

TABLE 3: SFG Vibrational Analysis for Nitro-OPE

observed frequency (cm ⁻¹)	(A _r ^{ssp} /A _r ^{ppp})	assignment	calculated (a _r) (∂α/∂Q)(∂μ/∂Q)/(10 ⁻²³ C ² m V ⁻¹ kg ⁻¹)					
			z'z'z'	x'x'z'	y'y'z'	x'z'x'	z'z'x'	x'x'x'
3067	0.29 ± 0.03	2 top	-3.9	-5.0	-0.4	0.0	0.5	0.7
3060	-0.07 ± 0.08	7a top	-7.9	1.1	0.0	0.0	0.9	0.0
2225	0.26 ± 0.10	C≡C asy ^a	132	-1.9	0.0	-0.7	-11.	0.1
2204	0.13 ± 0.04	C≡C sym ^b	-209	-3.4	0.0	-3.5	47	0.8
1615	0.05 ± 0.04	8a + NO ₂ asy	-46	0.4	0.0	-1.2	24	-0.2
1598	0.04 ± 0.06	8a top	-41	1.4	0.0	0.0	10.	-0.4
1582	0.03 ± 0.04	8a bot	-22	0.3	0.0	-1.4	14	-0.2
1546	0.02 ± 0.05	8a + NO ₂ asy	125	-4.4	-0.2	2.0	-55.	1.9
1509	0.00 ± 0.06	19a	-19	0.4	0.0	0.0	-0.2	0.0
1472	0.23 ± 0.08	19a	8.8	0.0	0.0	0.0	-2.0	0.0
1344 ^c	-na-	NO ₂ sym	0.7	1.0	0.0	-5.7	11.	16
1142	0.15 ± 0.03	18a m + CN	-2.6	-0.2	0.0	-1.3	25	1.6
1067	-0.03 ± 0.02	18a b + CS	-5.8	-1.0	0.0	-0.2	1.8	0.3
1024	0.25 ± 0.16	18a top	-1.4	-0.4	0.0	0.0	0.0	0.0
1010	-irr-	18a bot	-5.4	-0.5	0.0	0.0	0.6	0.0
996	-irr-	12 top	2.2	0.3	0.0	0.0	0.0	0.0

^a Localized mostly on the top C≡C. ^b Localized mostly on the bottom C≡C. ^c Frequency from bulk IR spectra, line not observed in SFG.

Therefore, all reported VR-SFG spectra were recorded on ≈1 cm² fragments freshly diced from a SAM-coated wafer stored in the dark under oil-free vacuum. All reported SE spectra were recorded on ≈1 cm² samples immediately upon removal from solution.

The VR-SFG spectra were acquired with a broad-bandwidth apparatus that has been described earlier.²⁵ In brief, broad-bandwidth (>150 cm⁻¹ fwhm) tunable IR pulses, derived from an ≈100-fs, 1-kHz, regeneratively amplified Ti-sapphire laser system were temporally and spatially overlapped with narrow-bandwidth (≈3 cm⁻¹) 794 nm (VIS) pulses at the sample. The reflected sum-frequency light was collected, dispersed with a 0.75 m spectrograph, and detected with a scientific grade CCD array detector. This allowed the simultaneous acquisition of a >300 cm⁻¹-wide SFG spectrum. In this work, the IR and VIS beam diameter and angle of incidence were typically 100 μm, 54° and 150 μm, 36°, respectively. The IR pulse energy varied from ≈4 μJ at 3 μm to ≈1 μJ at 10 μm while the VIS pulse energy was typically 2 μJ. The displayed spectra were normalized by the response of a reference sample that corrects for the intensity envelope of the broad-bandwidth IR pulse. An automated carousel was used to position the reference and up to five samples under the incident beams. SSP spectra (S-polarized sum, S-polarized vis, P-polarized IR²⁶) typically are the average of 10 to 20 sample/reference ratios with acquisition time per sample of ≈240 s. PPP spectra typically are the average of three sample/reference ratios with acquisition time per sample of ≈60 s. At IR wavelengths of ≈3 μm, z-cut quartz was used as the reference; at ≈5 μm, z-cut quartz and as-received Au were used; at long wavelengths, as-received Au was used. (As-

received Au films were vapor-deposited films of >100 nm on Cr-primed Si substrates.) The quartz was unusable as a reference in the 6 μm to 10 μm range due to resonant structure. All spectra are scaled to the respective signal from the as-received Au reference, calibrated to quartz at 5 μm. The x-axis is the IR wavenumber, to allow easy comparison with linear vibrational spectroscopies.

The SE spectra were acquired with a J. A. Woollam Co. M-2000D²⁷ rotating compensator ellipsometer over the wavelength range 190 nm to 1000 nm and at an angle of incidence of 70°. The spectra were zone-averaged and represent a total of ≈100 s signal acquisition.

3. Results

3.1 VR-SFG. Shown in Figure 1 are SFG spectra for OPE and nitro-OPE films at central IR wavelengths of about 3 μm, 5 μm, 6 μm, and 10 μm. As described in Appendix I, the SFG spectra can be fit to the coherent superposition of a series of Lorentzian lines and a nonresonant background. Also shown in Figure 1 are weighted nonlinear least-squares fits of the PPP spectra to eq 5 and the SSP spectra to eq 4. The PPP and SSP spectra were fit simultaneously with the constraint that ν_r and Γ_r were the same for the two spectra. The results for the principle lines are summarized in Tables 2 and 3. Also presented in Tables 2 and 3 are assignments for the observed lines, based on comparison with IR and Raman spectra of the parent compounds and DFT calculations (see Supporting Information). Wilson notation for the fundamental modes of 1,4-substituted benzene is used.^{28,29} Modes that are localized to a single ring are labeled

top, mid, or bot. Modes that are concerted motions distributed across the three rings carry no additional label. The observed frequencies are in good agreement with IR reflection spectra of similar films.²¹

The spectra of the two molecules are qualitatively similar and dominated by modes polarized along the chain axis. This is due to both a near-vertical orientation of the molecules and the intrinsic oscillator strengths (see below). The principal differences in the spectra are found in the presence of the NO₂ asymmetric stretch near 1547 cm⁻¹ in the nitro-OPE and in the different phases (destructive interference is observed for nitro-OPE, while constructive interference is evident for OPE) of the strong C≡C symmetric stretch near 2200 cm⁻¹, the 8a derived mode near 1581 cm⁻¹, and the 18a mode near 1142 cm⁻¹. As shown in Figure 2, negligible intensity was found at the expected position of the NO₂ symmetric stretch (~1340 cm⁻¹) for the nitro-OPE films. This is not due to an intrinsically weak oscillator. The symmetric stretch was quite strong in SAMs of *p*-nitrobenzenethiol (PNBT), which is also shown in Figure 2.

The VR-SFG spectrum carries information about the chemical identity of the adsorbed species (via the vibrational frequencies) and their orientation (via the phase and amplitude of the resonant features).^{30–35} The extraction of orientation information can be done by either comparing relative mode intensities in a single spectrum^{36,37} or by comparing the ratios of mode intensities in spectra acquired with different polarization configurations.^{38–40} In either case, one must be able to estimate the components of the molecular hyperpolarizability β that determine the observed susceptibility χ (see Appendix I). Unlike conventional IR absorption, β cannot be directly calibrated by measurements on bulk samples unless a polar ordered molecular crystal is available. When comparing relative mode intensities, the accuracy of the analysis is directly proportional to the accuracy of the estimated elements of β . When comparing different polarization combinations, one is sensitive only to the relative accuracy of the elements of β on a per-mode basis. However, the analysis requires an accurate determination of the Fresnel coefficients and local fields.⁴⁰ When neither the SUM nor VIS frequencies are near resonances in the molecule, β can be approximated by

$$\beta_{ijk}^{\text{nr}} = \beta_{ijk}^{\text{nr}} + \sum_r \frac{(a_r)_{ijk}}{(\nu - \nu_r + i\gamma_r)}$$

$$(a_r)_{ijk} = \frac{1}{8\pi^2 c^2 \nu_r \epsilon_0} (a_r)_{ijk}$$

$$(a_r)_{ijk} = \frac{\partial \alpha_{ij} \partial \mu_k}{\partial Q_r \partial Q_r} \quad (1)$$

where β_{ijk}^{nr} is the nonresonant part of β , $(\partial \alpha_{ij} / \partial Q_r)$ is the Raman polarizability derivative, and $(\partial \mu_k / \partial Q_r)$ is the infrared transition dipole moment of vibrational mode r with wavenumber ν_r .⁴¹ In most studies, the elements of β were estimated from additive bond polarizability models for $(\partial \alpha_{ij} / \partial Q_r)$ and $(\partial \mu_k / \partial Q_r)$.^{41–43} In this study, we have used quantum chemical calculations of $(\partial \alpha_{ij} / \partial Q_r)$ and $(\partial \mu_k / \partial Q_r)$. Density functional theory calculations were performed with the B3-LYP hybrid functional^{44,45} and a 6–31/G** basis set with the Gaussian 98 program.^{27,46}

There are 27 elements in (a_r) ; however, the approximate molecular symmetry significantly simplifies the tensor. Presented in Tables 2 and 3 are the calculated values of (a_r) for the parent thiol compounds. In the calculations, the CCSH

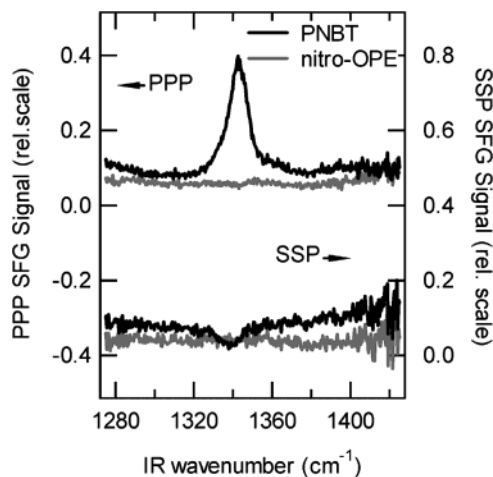


Figure 2. SFG spectra of the NO₂ symmetric stretch region for nitro-OPE and PNBT.

dihedral angle was constrained to place the CSH plane perpendicular to the plane of the rings (see Table 1). This is not the calculated ground state of the isolated thiols (which has the CSH plane parallel to the plane of the rings; see Discussion). For OPE (Table 2), the calculated minimum energy structure is linear with all the rings in a common plane, resulting in a molecular symmetry of C_s; however, the (a_r) for the observed modes approximately obey C_{2v} symmetry; i.e., there are only five significant elements assuming Kleinman symmetry⁴⁷ for the vis and sum indices. Taking the z' axis to be along the chain axis and the x' axis to lie in the plane of the rings, the five elements of $(a_r)_{ijk}$ have ijk : $z'z'z', x'x'z', y'y'z', x'z'x' = z'x'x', y'z'y' = z'y'y'$. The out-of-plane elements ($y'y'z'$ and $y'z'y'$) are very weak. For isolated nitro-OPE (Table 3), the calculated ground state has the rings and NO₂ nominally coplanar; however, the chain is “bent” by $\approx 6^\circ$ about the central ring (see Table 1). The out-of-plane elements are again very weak so that only the six elements in the plane are significant. Taking the z' axis to be the director from the center to top ring, and the x' axis to be in the plane of the rings, the six relevant elements of $(a_r)_{ijk}$ have ijk : $z'z'z', x'x'z', x'z'x' = z'x'x', z'z'x', z'x'z' = x'z'z',$ and $x'x'x'$. It is interesting to note that the strong features in the VR-SFG spectra of the two molecules correspond to the strongly Raman active modes; therefore, the spectra are complementary to the IRAS spectra reported in ref 21. For example, in both OPE and nitro-OPE, the IR feature due to 19a, near 1513 cm⁻¹, is strong, but the C≡C stretches are weak. In the VR-SFG spectra, the C≡C stretches are strong, as are the 8a-derived features near 1600 cm⁻¹.

For thin films on metallic surfaces, a surface selection rule arises due to the strong screening of the IR driving field, and only PPP and SSP polarization combinations give quantifiable spectra. As shown in Appendix I (eq 8), the ratio of the line amplitudes ($A_r^{\text{ssp}}/A_r^{\text{ppp}}$) provides information on the two surface susceptibility elements χ_{zzz} and χ_{xxz} and, via β_{ijk} , insight into the molecular orientation distribution $f(\theta, \phi, \psi)$, where θ, ϕ, ψ are the Euler angles relating the lab and molecular frames, defined in Figure 3. However, the experiment does not allow complete determination of f ; therefore, a trial orientation distribution with limited flexibility must be assumed. The experimentally derived ($A_r^{\text{ssp}}/A_r^{\text{ppp}}$) ratios are presented in Tables 2 and 3. Each ratio is the average of two to four values obtained from spectra recorded for independently diced samples. A positive sign for the ratio indicates similar phase with respect to the nonresonant background (for example, destructive in both spectra), whereas a negative sign indicates opposite behavior

TABLE 4: Optical Parameters Used in SFG Analysis^a

$\nu_{\text{IR}} \text{ (cm}^{-1}\text{)}$	$n_{\text{Au}}[\nu_{\text{IR}}]$	$n_{\text{Au}}[\nu_{\text{SUM}}]$	F_{ssp}	F_{zzz}	F_{xxz}	$F_{\text{zxx}} + F_{\text{zxx}}$
3060	$1.87 + 20.2i$	$0.18 + 3.00i$	$0.206 \exp(-2.53 \text{ I})$	$0.310 \exp(0.77 \text{ I})$	$0.311 \exp(0.86 \text{ I})$	$0.020 \exp(0.96 \text{ I})$
2210	$3.23 + 27.9i$	$0.16 + 3.55i$	$0.179 \exp(-2.60 \text{ I})$	$0.314 \exp(0.68 \text{ I})$	$0.269 \exp(0.76 \text{ I})$	$0.009 \exp(0.87 \text{ I})$
1546	$5.88 + 38.8i$	$0.16 + 4.07i$	$0.159 \exp(-2.65 \text{ I})$	$0.313 \exp(0.62 \text{ I})$	$0.238 \exp(0.69 \text{ I})$	$0.003 \exp(0.83 \text{ I})$
1342	$7.53 + 43.7i$	$0.16 + 4.20i$	$0.154 \exp(-2.66 \text{ I})$	$0.312 \exp(0.60 \text{ I})$	$0.231 \exp(0.67 \text{ I})$	$0.003 \exp(0.83 \text{ I})$
1070	$11.3 + 52.7i$	$0.16 + 4.39i$	$0.149 \exp(-2.68 \text{ I})$	$0.311 \exp(0.58 \text{ I})$	$0.222 \exp(0.65 \text{ I})$	$0.002 \exp(0.85 \text{ I})$

^a $n_{\text{Au}}[\nu_{\text{VIS}}] = 0.18 + 5.06i$; film $n_e = 1.5$; film thickness 2.0 nm.

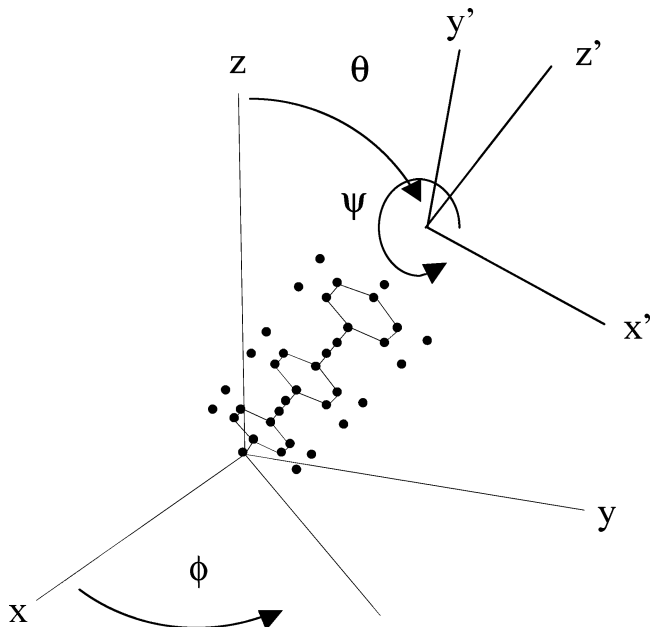


Figure 3. Definition of Euler angles and orientation of adsorbed OPE. The molecule (x',y',z') frame is defined such that the rings line in the $x'-z'$ plane, and z' is along the long axis of the molecule.

in the two spectra. If one assumes a delta-function orientation distribution for both θ and ψ , the ($A_r^{\text{ssp}}/A_r^{\text{ppp}}$) ratios for a single mode become a function of three parameters: θ , ψ , and n_e (the effective index of refraction for the molecular film). Inspection of Table 2 establishes that, except for ν_2 at $\approx 3068 \text{ cm}^{-1}$, all the observed modes for OPE are dominated by a single resonant hyperpolarizability element ($a_{rzz'z'}$) and appear cylindrically symmetric. Therefore, they provide no information about ψ . Table 4 indicates that the Fresnel factors that link A to (a_r) are weakly dispersive, such that all modes except ν_2 should have the same ($A_r^{\text{ssp}}/A_r^{\text{ppp}}$) ratio. This is supported by the data for all modes except those attributed to ν_{19a} . The source of this discrepancy is not known. We have performed a weighted, nonlinear least squares (NLS) fit to the ($A_r^{\text{ssp}}/A_r^{\text{ppp}}$) ratios for modes 7a, C \equiv C, 8a, and 18a (total of 7 ratios) to determine θ as a function of n_e . In the fit, all elements of (a_r) are used, a delta function distribution in θ is assumed, and both ψ and ϕ are averaged over a uniform distribution. It has been observed that n_e typically lies between the index of the ambient (air) and the film.^{40,48} As n_e is varied from 1.1 to 1.7, θ varies from 52 to 28° (see Figure 4). Inclusion of ν_2 in the analysis allows a determination of ψ for fixed n_e or a determination of n_e for a known ψ distribution. If we use $\theta[n_e]$ from the other modes in the analysis of ν_2 , we find physical solutions only for n_e in the range 1.2–1.7, resulting in $\psi[\theta[n_e], n_e]$ as shown in Figure 4A. Because n_e is not accurately known, determination of ψ is problematic. It has been suggested, on the basis of STM images,^{12,16} that the OPE unit cell contains two molecules, due to the adoption of a herringbone structure. If one assumes two molecules per unit cell with ψ and $\psi + 90^\circ$, the resultant

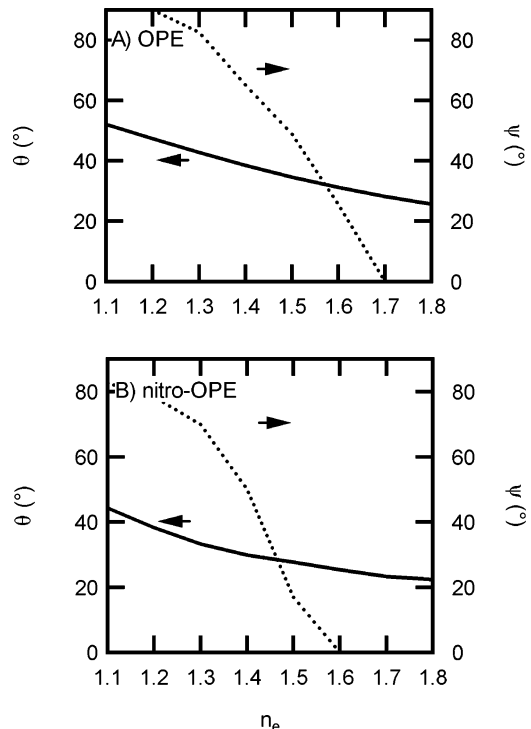


Figure 4. θ vs n_e from analysis of cylindrically symmetric modes (solid lines). ψ vs n_e from inclusion of ν_2 in the analysis (dotted lines). See text for details.

average becomes essentially independent of ψ for θ in the range: 0° to 60° . In this case, a weighted nonlinear least-squares fit to the data for all modes in Table 2 (excluding 19a) results in $\theta = 34^\circ \pm 10^\circ$, $n_e = 1.55 \pm 0.25$.⁴⁹ This tilt angle is in good agreement with the value of 32° based on IRAS.²¹

Inspection of Table 3 establishes that except for the ν_2 C–H stretch at $\sim 3067 \text{ cm}^{-1}$ and the NO_2 sym stretch at 1344 cm^{-1} , all the observed modes for nitro-OPE are dominated by ($a_{rzz'z'}$) or ($a_{rzz'x'}$). As can be seen from eq 7, the ratio of χ_{xxz} to χ_{zzz} is independent of ψ for narrow distribution functions when only $z'z'z'$ and $z'z'x'$ are dominant; therefore, as was the case for OPE, the majority of the observed modes should have the same ($A_r^{\text{ssp}}/A_r^{\text{ppp}}$) ratio and provide information only on θ . The ($A_r^{\text{ssp}}/A_r^{\text{ppp}}$) ratios for ν_{19a} are in better agreement with expectation than for OPE; however, the feature at 1472 cm^{-1} is still problematic. A weighted NLS fit to the ($A_r^{\text{ssp}}/A_r^{\text{ppp}}$) ratios for modes 7a, C \equiv C(asy), C \equiv C(sym), 8a, 8a + NO_2 asy, and 18a (total of 10 ratios) to determine θ as a function of n_e results in Figure 4b. As with OPE, inclusion of ν_2 in the analysis allows a determination of ψ for fixed n_e , or a determination of n_e for a known ψ distribution. Physical solutions exist only for n_e in the range 1.1–1.6, resulting in $\psi[\theta[n_e], n_e]$ as shown in Figure 4b. As with OPE, if one assumes two molecules per unit cell in a herringbone structure with ψ and $\psi + 90^\circ$, the resultant average becomes essentially independent of ψ . In this case, a weighted NLS fit to the data for all modes in Table 3 (excluding 19a) results in $\theta = 22^\circ + 18 - 22^\circ$, $n_e = 1.45 \pm 0.3$.⁴⁹

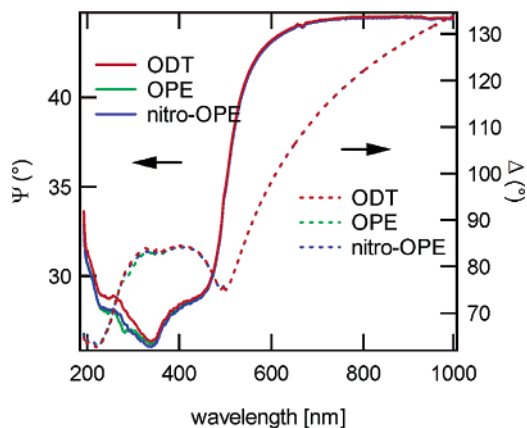


Figure 5. Ellipsometric parameters Ψ (left axis) and Δ (right axis) for OPE, nitro-OPE, and ODT films.

It is interesting to note that the calculated (a_r) for the NO_2 symmetric stretch does not correspond to a C_{2v} symmetry group hyperpolarizability oriented along the C–N bond, that is, $(a_r)_{lmn} \neq (a_r^{C_{2v}})_{ijk} R_{il} R_{jm} R_{kn}$ with R the transformation matrix for a rotation of 120° about y' . Instead, (a_r) reflects a rotation of only 90° , and $(a_r)_{xxx}$ is dominant. This is orthogonal to the majority of the observed modes and should provide considerable insight into the nitro-OPE ψ . Unfortunately, the mode is unobservable in SSP and cannot be analyzed as above. If we assume that the quantum chemical calculation accurately predicts the ratio of the a_r for the NO_2 group in PNBt and nitro-OPE, the ratio of the observed features in the PPP spectra in Figure 2 can be used to estimate ψ . Including $(A_{\text{nitro-OPE}}^{\text{PPP}}/$

$A_{\text{PNBT}}^{\text{PPP}}$) for the symmetric stretch along with the other 11 ratios in the NLS fit results in $\psi = 60^\circ \pm 20^\circ$, $\theta = 27^\circ \pm 13^\circ$, $n_e = 1.35 \pm 0.3$.

3.2 SE. Shown in Figure 5 are SE spectra (ellipsometric angles⁵⁰ Ψ and Δ) for OPE, nitro-OPE, and octadecanethiol (ODT) SAMs. For thin films, Δ is most sensitive to thickness. The similarity of Δ at long wavelengths for the three samples indicates that all three of the films have comparable optical thickness. The fine structure in Ψ for the OPE and nitro-OPE films in the UV indicates absorption by the films. Quantitative analysis of the SE spectra requires determination of the index of refraction of the vapor-deposited Au substrates because it depends sensitively on the conditions of the deposition. The films in Figure 5 were formed on three adjacent $\approx 1 \text{ cm}^2$ chips diced from the center of a wafer. The pseudodielectric function ϵ_{Au} for the Au film was calculated from the ODT sample, assuming the ODT film was 2.3 nm thick and had an index of refraction $n = \sqrt{\epsilon}$ given by a Cauchy dispersion: $1.50 + 0.001/(1 + \lambda^2)$, with λ the visible wavelength in micrometers.⁵¹ This procedure incorporates the effects of the thiol–Au interaction into the Au substrate pseudodielectric function.⁵² ϵ_{Au} was then used to estimate the film thickness for the OPE and nitro-OPE films using the data between 1000 and 600 nm. For ultrathin films, film thickness and dielectric constant ϵ_{film} are not experimentally separable⁵³ such that ϵ_{film} must be obtained from other data to determine the thickness. In previous studies of OPE, values for n between 1.46¹³ and 1.55¹ have been assumed. These values are low compared to recent determinations of n for model poly(arylene–phenylene),⁵⁴ poly(phenylene–vinylene),⁵⁵ and poly(phenylene–ethynylene)⁵⁶ films that range between 1.55 and 1.8, in reasonable accord with estimates of

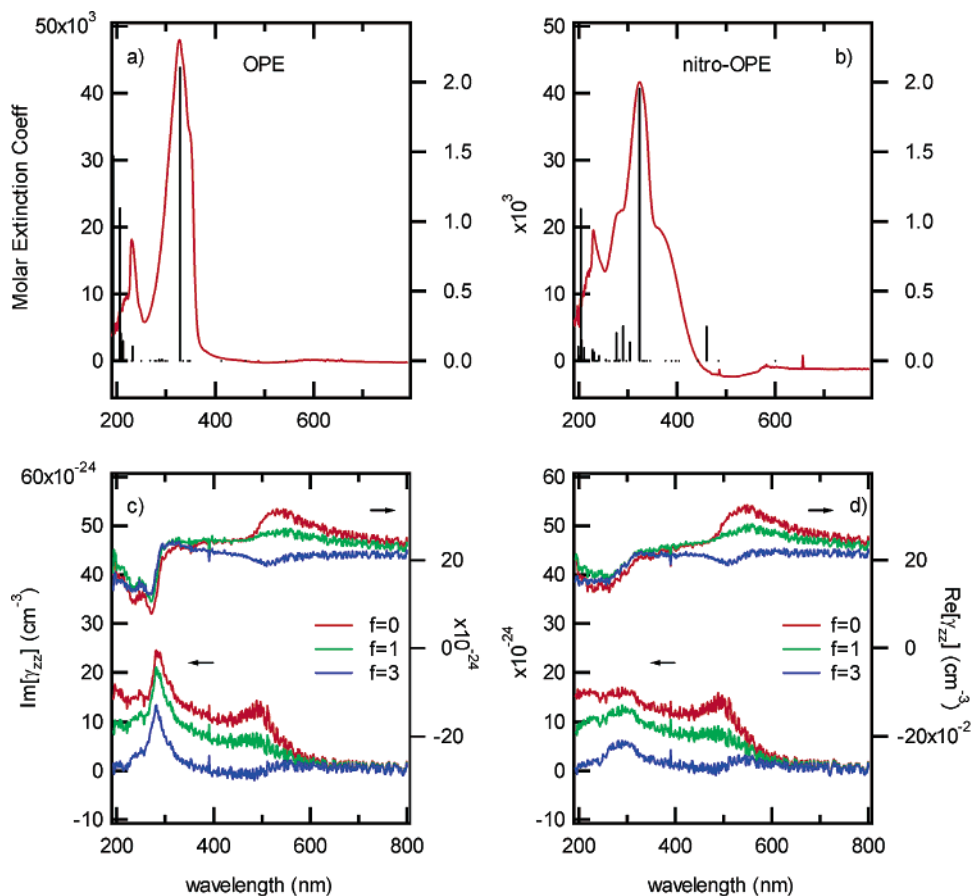


Figure 6. UV–vis absorption spectra (left axis) and theoretically calculated electronic spectra (right axis) for (a) OPE and (b) nitro-OPE. Derived effective polarizability $\gamma_{zz}(4\pi\epsilon_0)$ as a function of the parameter f (see text) for (c) OPE and (d) nitro-OPE.

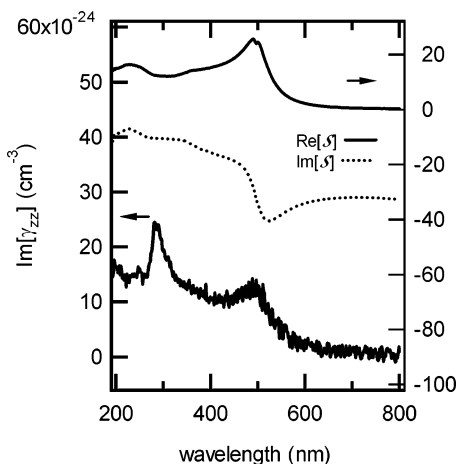


Figure 7. SE sensitivity factor (see text) and extracted volume polarizability for OPE.

≈ 1.75 from a QSAR calculation.²¹ Assuming n is 1.67 (the center of the range 1.55–1.8), the derived thickness for three independently prepared OPE, nitro-OPE, and ODT sets were OPE, $1.8 \text{ nm} \pm 0.1 \text{ nm}$; nitro-OPE, $1.93 \text{ nm} \pm 0.07 \text{ nm}$.⁵⁷ These thicknesses are consistent with earlier reports and are comparable to the calculated length of the molecules (S to terminal H distance of 1.95 nm), suggesting a densely packed film.

Shown in Figure 6a and b are the molar extinction coefficients for the OPE (thiol) and nitro-OPE (thioacetate), measured in CH_2Cl_2 . Also shown in Figure 6 are the scaled calculated oscillator strengths and transition frequencies from a ZINDO/S, CI singles calculation of the excited states for the respective thiol.⁵⁸ The principle features in the absorption spectra near 320 nm for both molecules are attributed to $\pi\pi^*$ transitions between extended states along the molecule and have transition dipole moments calculated to lie along the z' axis. In OPE, the transition corresponds to $S_0 \rightarrow S_1$. The calculated short wavelength feature ($\approx 190 \text{ nm}$) in both molecules is also polarized along z' , while the slightly longer wavelength feature ($\approx 204 \text{ nm}$) is polarized along the x' axis. The shoulders at 280 nm and 370 nm for the nitro-OPE are attributed to transitions involving the NO_2 and have transition dipole moments in the $x'-z'$ plane. The transitions in the short-wavelength shoulder (304 nm, 289 nm, 276 nm) are nominally polarized along the C–N bond, whereas the long-wavelength shoulder (460 nm) is polarized perpendicular to the C–N bond.

The ellipsometric data presented in Figure 5 could be inverted to obtain the isotropic pseudodielectric constant ϵ for the adsorbed film, assuming a thickness. However, given the high

degree of orientation in the film indicated by the VR-SFG and earlier IRAS²¹ and the calculated transition dipole moments, an anisotropic model is clearly necessary to describe the system. In general, the two parameters measured in SE (Ψ and Δ) cannot determine the five parameters of a uniaxial dielectric function (Re and Im parts of ϵ_{xx} and ϵ_{zz} and thickness) without additional assumptions. Instead of using the usual dielectric function and thickness, the optical response of a uniaxial thin film can be parametrized by two complex lengths or “ d parameters”.⁵⁹ This formalism has been developed to facilitate the description of the optical response of clean metal surfaces, because it straightforwardly allows for the treatment of the continuous decay of the metal density into the vacuum.^{60,61} As detailed in Appendix II, d -parameter theory can be used to clearly identify the physical origin of ellipsometric contrast in terms of the weighted effective polarizability difference, $\epsilon_{\text{Au}}\gamma_{zz} - \gamma_{xx}$, where γ is the average volume polarizability tensor for the film. γ contains the effects of local fields, intermolecular coupling, and image dipoles. In the limit of a noninteracting array of molecules, with no images, γ is the conventional molecular volume polarizability $\alpha/(4\pi\epsilon_0)$. For a high-dielectric material such as a metal, we adopt the surface selection rule approximation that $\epsilon_{\text{Au}}\gamma_{zz} - \gamma_{xx} \approx \epsilon_{\text{Au}}\gamma_{zz}$ and directly invert the SE data to obtain the Re and Im parts of γ_{zz} using eq 14. The results are shown in Figure 6c and d. To assess the validity of this treatment, we have also calculated γ_{zz} assuming that the ratio $f \equiv \gamma_{xx}/\gamma_{zz}$ is 1 or 3. The results are also shown in Figure 6c and d and indicate that the significant features of the polarizability, both the magnitude of the real component at long wavelengths and the position of the principle features at short wavelengths, are robust to the assumptions of f . From Figure 6, we see that the dominant resonant feature in γ_{zz} (due to the strong $\pi\pi^*$ transition) is significantly blue-shifted from the position in solution. For OPE, the resonance shifts from 327 nm to 286 nm, whereas in nitro-OPE, the resonance shifts from 325 nm to 294 nm. A similar blue shift was reported on the basis of transmission measurements on OPE adsorbed on semitransparent Au films.⁷

The structure in the calculated γ_{zz} for both OPE and nitro-OPE near 500 nm is attributed to artifacts due to small differences between the Au optical constants of the test films and the ODT-covered calibration films. This is supported by Figure 7, in which γ_{zz} is compared to the “sensitivity” function S relating the observed reflectivity difference to γ_{zz} (see eq 14). The strong dispersion in the Au results in a peak in the sensitivity near 500 nm.

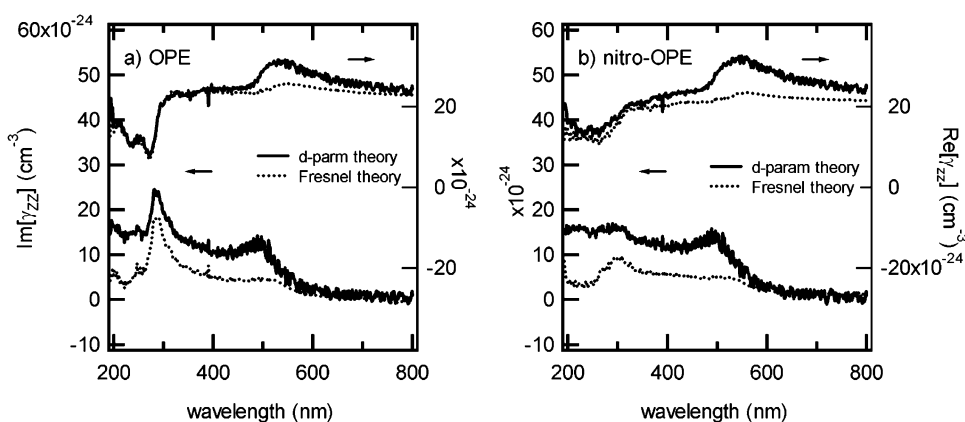


Figure 8. Comparison of γ_{zz} obtained directly from the SE data using the surface selection rule and γ_{zz} obtained from a uniaxial analysis of the data using Fresnel theory (see text) for (a) OPE and (b) nitro-OPE.

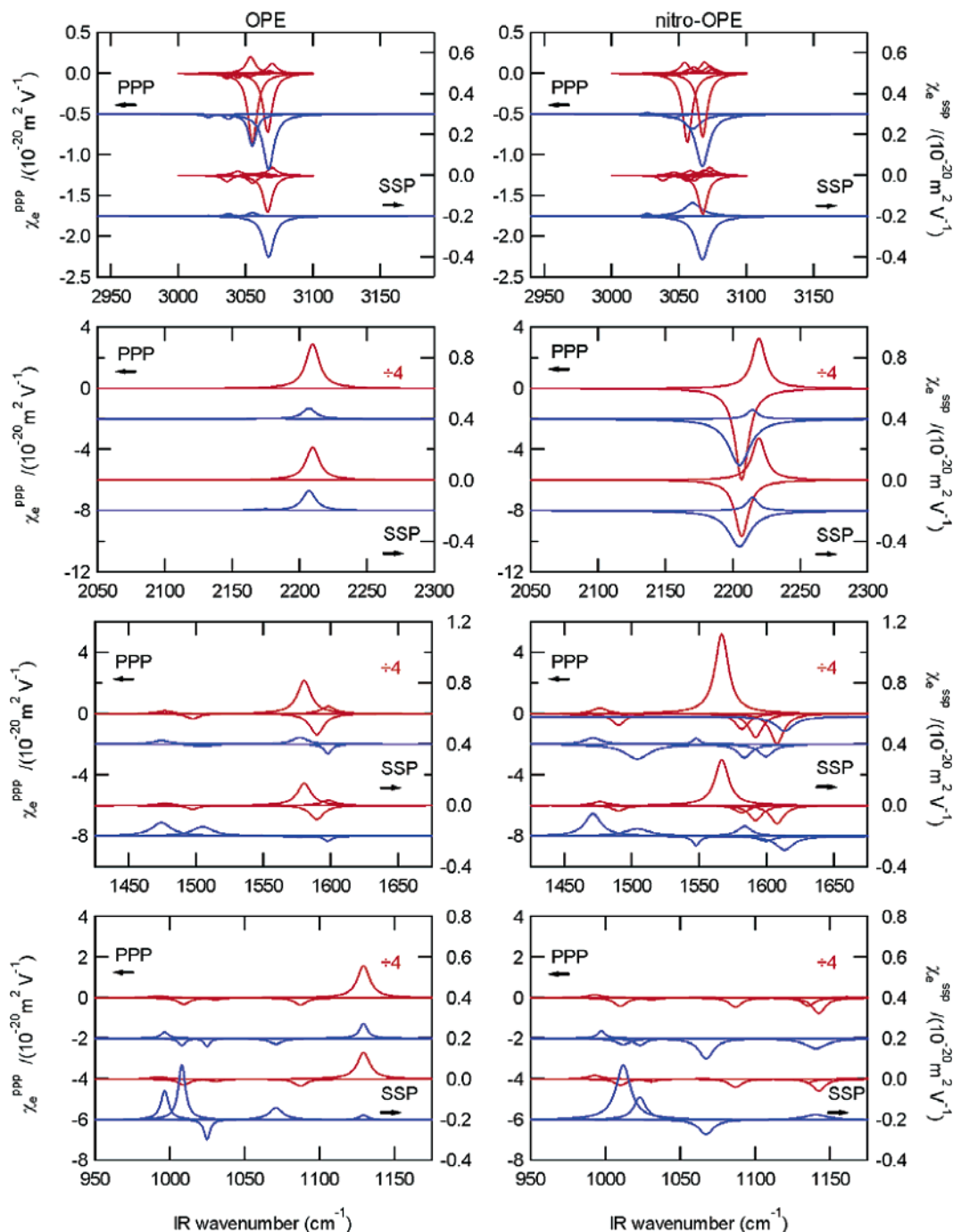


Figure 9. Comparison of the imaginary parts of the resonant components of the SFG spectra (blue from Figure 1) and the imaginary parts of the theoretically calculated hyperpolarizability components (red) for OPE (left column) and nitro-OPE (right column). The DFT frequencies have been scaled by 0.954, 0.959, 0.962, and 0.978 for the 3000, 2200, 1500, and 1000 cm^{-1} regions, respectively. The theoretical χ 's are scaled by 0.25 for the 2200, 1500, and 1000 cm^{-1} regions, respectively.

To our knowledge, the use of d -parameter theory and the surface selection rule to obtain the real and imaginary parts of the surface polarizability γ is novel to this paper. Fresnel theory is more often used to interpret ellipsometric data.⁶² As discussed above, multiple assumptions must be made to develop a uniaxial model for an ultrathin film. The equivalence of the simple d -parameter approach and Fresnel theory is shown in Figure 8a and b, where γ_{zz} determined from the d -parameter approach is compared to γ_{zz} determined from Fresnel theory and the assumptions that the molecular film is 2 nm thick, that only ϵ_{zz} is dispersive, and that ϵ_{xx} is 1.42. The two approaches provide similar results; however, the d -parameter approach is far simpler.

4. Discussion

4.1 Molecular Orientation. Quantum chemical calculations of hyperpolarizabilities have been used to qualitatively guide the interpretation of VR-SFG,^{63,64} but have rarely been used for quantitative analysis.⁶⁵ The relatively good agreement between the determined values for θ from VR-SFG and earlier IRAS²¹ indicate that in this case, calculated hyperpolarizabilities allow quantitative analysis. This is supported by Figure 9, in which calculated and experimental values for $-\text{Im}[A_r/(\nu - \nu_r + i\Gamma_r)]$ are compared. The orientation average was performed for $f(\theta, \psi, \phi) = \delta(\theta - 30^\circ)\delta(\psi - 45^\circ)$, the DFT frequencies were scaled as indicated in the figure caption, and a surface

coverage of $4.5 \times 10^{14} \text{ cm}^{-2}$ was assumed. Only the zzz and xxz contributions to A^{PPP} were included in the calculation. There is excellent agreement between theory and experiment on the relative phases of the lines. In particular, the phase flips between OPE and nitro-OPE for the features at 1146 cm^{-1} , 1581 cm^{-1} , and 2204 cm^{-1} in the nitro-OPE spectra are predicted by theory. There is qualitative agreement on the relative mode intensity. The calculations agree well with the intensity of the C–H stretch features, but they overestimate the intensity of the fingerprint region features by ~ 4 . A similar disparity between the C–H stretch region and the fingerprint region is seen in the calculated Raman intensities (see Supporting Information).

The predicted VR-SFG spectra for calculations in which the SH bond lies in the plane of the rings (the calculated ground state) do not agree as well with the experimental spectra (see Supporting Information). The phase for the lines at 1581 cm^{-1} and 2204 cm^{-1} for OPE is not properly accounted for. The physical origin of the correlation between phase and the CSH bond angle is not known. However, the $\approx 97^\circ$ CSH bond angle results in some interaction between the thiol H and bottom ring H's, manifest in the C–H stretch normal modes. This results in a strong additional C–H stretch feature corresponding to a local mode of the C–H adjacent to the S–H. This feature is not present in the experimental spectra, as expected, due to the loss of H upon formation of the thiolate–Au bond. The large covalent radius of Au and the near linear bond angle implied by the observed moderate tilt indicate that there should be little C–H/Au interaction and the SH perpendicular calculation should better represent the perturbation of the molecule by adsorption than the SH in-plane calculation, consistent with observation.

The nominal tilt angle of 30° for both molecules is consistent with the tilt angle found for benzenethiol⁶⁶ and similar rigid rod-conjugated thiols.²⁰ Robust determination of the twist angle ψ for the OPE is problematic. The VR-SFG results are equally consistent with the reported 31° ψ for a primitive unit cell in ref 21 and an orthogonal herringbone structure at an arbitrary ψ . The lower symmetry of the nitro-OPE results in a more definitive analysis. Although it is likely that additional errors are introduced by the assumption that the calculated a_r 's for PNBT and nitro-OPE are relatively accurate, the tilt obtained by including the NO_2 sym stretch data, $\theta \approx 27^\circ$, is in good agreement with that determined by IRAS²¹ ($\theta \approx 32^\circ$). Similarly, the twist angle $\psi \approx 60^\circ$ is consistent with that found by the IR analysis of the non-nitro-containing modes ($\psi \approx 69^\circ$).⁶⁷ Second-order nonlinear optical techniques probe higher moments of the orientation distribution than linear techniques. Combination of measurements by both techniques can be used to determine both the mean and the width of the orientation distribution.⁶⁸ The good correlation between the VR-SFG data and IRAS data²¹ implies narrow θ distributions.

Both the OPE and nitro-OPE thiols have significant calculated dipole moments: $8.3 \times 10^{-30} \text{ C m}$ (2.5 D) and $1.8 \times 10^{-29} \text{ C m}$ (5.3 D), respectively. The repulsive energy for a vertically oriented array of dipoles is significant: $\approx 25 \text{ kJ mol}^{-1}$ for OPE at $4.5 \times 10^{14} \text{ cm}^{-2}$ density. This repulsion is lowered as the molecules tilt. The molecular dipole should lie along the z' axis for OPE and the dipole–dipole interaction will be a function of θ only, such that the twist angle will be defined by the $\pi\pi$ and van derWaals interactions between adjacent molecules. For nitro-OPE, the molecular dipole will be tipped off the z' axis, and the dipole–dipole interaction will depend on both θ and ψ . The equilibrium θ and ψ , thus, represents a compromise among dipole–dipole interactions, $\pi\pi$ and van derWaals

interactions, and possibly weak NO–H–C hydrogen bonding. It would seem probable that the nitro-OPE will therefore adopt a different packing geometry than OPE.

4.2 Electronic Excitations. Insight into the electronic structure of the adsorbed films is afforded by the determined volume polarizability γ . For OPE, the location of the main transition near 300 nm shows a significant blue shift, from 327 nm in solution to 286 nm in the film. The blue shift of the main transition to 286 nm is consistent with the formation of a molecular exciton due to dipole–dipole coupling between the transition dipoles of the film, as is commonly encountered in dye aggregates.⁶⁹ Similar blue-shifted transitions have been observed for nearly vertically oriented films of sexithiophene.⁷⁰ Simple models have been developed for the molecular excitons in linear⁷¹ and 2D arrays.⁷² When the transition dipole is nominally perpendicular to the line of centers of the molecules, the allowed exciton transition is blue-shifted, whereas if the transition dipole lies in the plane of the molecules, the transition is red-shifted. For a square array, the shift in the transition frequency is given by $\Delta\nu = (4.2/\hbar c)(M^2/4\pi\epsilon_0\eta^3)(3 \cos^2 \theta - 1)$, where ν is in cm^{-1} , \hbar is Planck's constant, c is the speed of light, ϵ_0 is the permittivity of free space, M is the transition dipole strength, and η is the lattice constant.⁷² From the molar extinction coefficient, we can estimate⁷³ M to be $3.0 \times 10^{-29} \text{ C m}$ (9.1 D) and obtain a tilt of 47° from the 4400 cm^{-1} observed shift and $\eta = 0.47 \text{ nm}$. The simple theory neglects the screening of the dipole interaction between the molecules and, thus, will overestimate the frequency shift (overestimate the tilt for $\theta < 54.7^\circ$); however, the qualitative agreement between the estimated tilt and the more robust values from VR-SFG and IR²¹ support the attribution of the blue shift. We note in passing that the feature at 230 nm in solution is not apparent (at wavelengths longer than 190 nm) in the absorbed film. This is consistent with a near upright orientation and the x' orientation of the transition dipole (surface selection rule forbidden).

The electronic spectra of adsorbed nitro-OPE show effects similar to that of OPE that again can be attributed to orientation and the formation of a molecular exciton. A similar blue shift (from 325 nm to 294 nm) is observed for the main transition, and the transition near 232 nm is not present. The data do not allow unambiguous assessment of the relative intensities of the NO_2 -derived shoulders. The most significant difference between nitro-OPE and OPE is in the total strength of the transitions, with the nitro-OPE being significantly weaker. This may simply reflect film quality and homogeneity. There is no evidence for significant perturbation of the electronic transitions of either molecule by interaction with the metal substrate.

5. Conclusions

The molecular orientation and dipole allowed electronic excitations of OPE and nitro-OPE films have been thoroughly characterized. VR-SFG is consistent with earlier IR analysis, suggesting both molecules are tilted by $\approx 30^\circ$ from the surface normal. For the nitro-OPE, it is suggested that the molecules are preferentially twisted by $\approx 60^\circ$. The optical transitions indicate strong intermolecular interactions, consistent with molecular exciton theory. There is no evidence for significant perturbation of the neutral electronic transitions by interaction with the substrate.

Acknowledgment. We thank Dr. Carlos Gonzalez for thoughtful discussion. C.S.Y., P.T.W., and C.A.H. were NIST National Research Council postdoctoral research associates.

J.M.T. thanks DARPA, ONR, NIST, and Molecular Electronics Corp. for financial support.

Supporting Information Available: Complete results from the quantum chemical calculations of the IR and Raman transition tensors, comparison of the calculated IR and Raman spectra with reference spectra of the parent compounds, normal mode displacements, and a detailed comparison of the predicted VR-SFG spectra for the two orientations of the SH bond. This material is available free of charge via the Internet at <http://pubs.acs.org>.

Appendix I

A number of authors have presented complete descriptions of orientation analysis based on VR-SFG data.^{30,38,41} This appendix is presented to clearly define the notation and model used. In classical, macroscopic theory, the electric field created at the sum frequency arises from an induced polarization P in a material. For a monolayer film system, there are three possible locations of this induced polarization: the molecular film, at the film/substrate interface, and in the bulk of the substrate. In general, the polarization at each location is given by

$$P_i(\omega_{\text{SUM}} = \omega_{\text{VIS}} + \omega_{\text{IR}}, r) = \epsilon_0 \chi_{ijk}^{\text{D}} E_j(\omega_{\text{VIS}}, r) E_k(\omega_{\text{IR}}, r) + \epsilon_0 \chi_{ijkl}^{\text{QIR}} E_j(\omega_{\text{VIS}}, r) \nabla_k E_l(\omega_{\text{IR}}, r) + \epsilon_0 \chi_{ijkl}^{\text{QVIS}} E_j(\omega_{\text{IR}}, r) \nabla_k E_l(\omega_{\text{VIS}}, r) + \epsilon_0 \nabla_j \chi_{ijkl}^{\text{Q}} E_k(\omega_{\text{VIS}}, r) E_l(\omega_{\text{IR}}, r) + \dots \quad (2)$$

where χ^{D} is the local dipole response and is expected to dominate the polarization when symmetry allowed. In locally centrosymmetric substrates, χ^{D} is symmetry-forbidden, and the leading order contributions come from the nonlocal, quadrupolar terms χ^{Q} .⁷⁴ The quadrupolar terms of the substrate can be written as effective surface dipole terms;⁷⁵ therefore, the superscript D will be omitted in the following.

The electric field at the sum frequency, arising from the induced polarization sheet, can be shown to be

$$E_1(\omega_{\text{SUM}}) = \frac{i\omega^2}{2\epsilon_0 c^2 k_z(\omega_{\text{SUM}})} \chi_{ijk}(\omega_{\text{SUM}} = \omega_{\text{VIS}} + \omega_{\text{IR}}) L_{il}^{\diamond}(\omega_{\text{SUM}}) L_{jm}(\omega_{\text{VIS}}) L_{kn}(\omega_{\text{IR}}) E_m(\omega_{\text{VIS}}) E_n(\omega_{\text{IR}}) \quad (3)$$

where $k_z(\omega_{\text{SUM}})$ is the component of the wavevector of the sum-frequency plane wave along the surface normal, L_{jm} and L_{kn} are conventional Fresnel transfer matrices relating the incident fields $E_{m,n}(\omega)$ to the fields at the nonlinear sheet, and L_{il}^{\diamond} is a transfer matrix for the emission of the sum-frequency. L_{il}^{\diamond} can be calculated by many routes; in this work, we use the Green's function approach of Sipe.⁷⁶ Local field effects are included in the spirit of ref 39 by allowing the polarization sheet to be imbedded in a thin film characterized by an effective index of refraction n_e . In the thin film limit,³⁹ this results in modification of the two-layer (ambient, substrate) L_{zz} by $L_{zz}(\text{three layer}) = L_{zz}(\text{two layer})(1/n_e)^2$. For Table 4, the full three-layer L is used, with the nonlinear source located midway into a layer 2 nm thick.

For an azimuthally symmetric sample, there are only four distinct elements in the nonlinear susceptibility χ_{ijk} : zzz , xxz = yyz , xzx = yzx , zxx = zxy . The three polarization combinations, SSP, SPS, and PSS, are each uniquely determined by the single χ elements xxz , xzx , and zxx , respectively. For each of these three polarization combinations, the normalized spectrum

can be modeled by

rel signal \equiv

$$\left| B'_{\text{nr}} + \sum_r \frac{A'_r e^{i\varphi}}{\nu - \nu_r + i\Gamma_r} \right|^2 = \frac{1}{|\chi_e|^2} \left| B_{\text{nr}} + \sum_r \frac{A_r e^{i\varphi}}{\nu - \nu_r + i\Gamma_r} \right|^2$$

$$\left| B_{\text{nr}} + \sum_r \frac{A_r e^{i\varphi}}{\nu - \nu_r + i\Gamma_r} \right|^2 = |F_{\text{nr}} \chi^{\text{nr}} + F \chi^{\text{res}}|^2 \quad (4)$$

where F_{nr} , χ^{nr} , F , and χ^{res} are the nonresonant and resonant total Fresnel factors ($F_{ijk} = L_{ii}(\omega_{\text{sum}}) L_{jj}(\omega_{\text{VIS}}) L_{kk}(\omega_{\text{IR}})$) and nonlinear susceptibilities of the sample, and χ_e is the effective susceptibility of the reference. B_{nr} arises from nonresonant contributions to χ^{nr} , and A_r , ν_r , and Γ_r are the amplitude, center wavenumber, and line width (hwhm), respectively, for vibrational mode r . The terms A_r , B_{nr} , and φ reflect both the relevant χ and the Fresnel factor weights. In the case of PPP polarization, the spectrum can be modeled by

rel signal \equiv

$$\left| B'_{\text{nr}} + \sum_r \frac{A'_r e^{i\varphi_r}}{\nu - \nu_r + i\Gamma_r} \right|^2 = \frac{1}{|\chi_e^{\text{PPP}}|^2} \left| B_{\text{nr}} + \sum_r \frac{A_r e^{i\varphi_r}}{\nu - \nu_r + i\Gamma_r} \right|^2$$

$$\sim |F_{\text{nr}} \chi^{\text{nr}} + F_{zzz} \chi_{zzz}^{\text{res}} + F_{xxz} \chi_{xxz}^{\text{res}} + F_{xzx} \chi_{xzx}^{\text{res}} + F_{zxx} \chi_{zxx}^{\text{res}}|^2 \quad (5)$$

The terms A_r and φ_r reflect the sum of contributions from all four χ elements. In the near copropagating configuration used in this study, the Fresnel factors F_{xxz} and F_{zxx} are approximately equal and opposite (see Table 4). Assuming pseudo-Kleinmann symmetry⁷⁷ holds for the sum and vis indices of χ^{res} , that is, $\chi_{xxz}^{\text{res}} \approx \chi_{zxx}^{\text{res}}$ these terms will nearly cancel in eq 5.

The macroscopic χ can be modeled as the orientation average of a molecular hyperpolarizability β , $\chi_{ijk} = N \langle \beta_{lmn} R_l R_m R_n \rangle$, where R is a rotation matrix relating the internal coordinates of the molecule to the lab coordinates and N is the number density. For a molecule of C_{2v} symmetry, the in-plane averaged χ elements that are observable on a metal substrate (zzz and xxz) can be shown to be

$$A_1: \chi_{zzz} = N(\beta_{x'x'z'} \langle \cos \theta \sin^2 \theta \cos^2 \psi \rangle + \beta_{z'z'z'} \langle \cos^3 \theta \rangle)$$

$$A_1: \chi_{xxz} = \frac{N}{8} (\beta_{x'x'z'} \langle \cos \theta (3 + \cos 2\theta - 2 \sin^2 \theta \cos 2\psi) \rangle + 4\beta_{z'z'z'} \langle \cos \theta \sin^2 \theta \rangle)$$

$$B_1: \chi_{zzz} = 2N\beta_{x'x'z'} \langle \cos \theta \sin^2 \theta \cos^2 \psi \rangle$$

$$B_1: \chi_{xxz} = -N\beta_{x'x'z'} \langle \cos \theta \sin^2 \theta \cos^2 \psi \rangle \quad (6)$$

For a molecule of C_s symmetry, the resulting expressions are very elaborate.⁷⁸ Retaining only the terms that are significant in the calculated β (see Tables 2 and 3: $z'z'z'$, $x'x'z'$, $x'z'x'$, $z'z'x'$, and $x'x'x'$) the in-plane averaged χ elements can be shown to be

$$\chi_{zzz} = N(-\beta_{x'x'x'} \langle \sin^3 \theta \cos^3 \psi \rangle + (\beta_{x'x'z'} + 2\beta_{z'z'x'}) \langle \cos \theta \sin^2 \theta \cos^2 \psi \rangle - (2\beta_{x'z'z'} + \beta_{z'z'x'}) \langle \cos^2 \theta \sin \theta \cos \psi \rangle + \beta_{z'z'z'} \langle \cos^3 \theta \rangle)$$

$$\begin{aligned} \chi_{xxz} = & \frac{N}{16}(-\beta_{x'x'x'}\langle \cos \psi \sin \theta (6 + 2\cos 2\theta - 4\sin^2 \theta \cos 2\psi) \rangle \\ & -\beta_{x'z'z'}\langle \cos \theta (6 + 2\cos 2\theta - 4\sin^2 \theta \cos 2\psi) \rangle \\ & -16\beta_{x'z'x'}\langle \cos \theta \sin^2 \theta \cos^2 \psi \rangle + 16\beta_{x'z'z'}\langle \cos^2 \theta \sin \theta \cos \psi \rangle \\ & -8\beta_{z'z'x'}\langle \cos \psi \sin^3 \theta \rangle + 8\beta_{z'z'z'}\langle \cos \theta \sin^2 \theta \rangle) \end{aligned} \quad (7)$$

The observed ($A_r^{\text{ssp}}/A_r^{\text{ppp}}$) were used to extract a trial orientation distribution function from

$$\frac{A_r^{\text{ssp}}}{A_r^{\text{ppp}}} = \frac{A_r^{\text{ssp}}}{A_r^{\text{ppp}}} \left| \frac{\chi_e^{\text{ssp}}}{\chi_e^{\text{ppp}}} \right| = \frac{F_{\text{ssp}} \chi_{xxz}^{\text{res}}}{F_{zzz} \chi_{zzz}^{\text{res}} + F_{xxz} \chi_{xxz}^{\text{res}} + (F_{xzz} + F_{xzz}) \chi_{xzx}^{\text{res}}} \quad (8)$$

given β_{ijk} from quantum chemical calculations (see text). This required determination of the ratio ($|\chi_e^{\text{ssp}}|/|\chi_e^{\text{ppp}}|$). For z-cut quartz, this ratio can be calculated⁴³ and is 1.1. For the Au film reference employed, this was found to be 0.32 ± 0.02 , independent of wavelength.

Appendix II

The change in the optical response of a planar interface, due to the presence of a molecular thin film, has been treated by numerous authors.⁷⁹ The d -parameter formalism^{59,61} provides a useful paradigm for comparing various models for monolayer films. To first order in the ratio of the effective film thickness to the wavelength of light, the s and p amplitude reflectivities can be described by

$$\begin{aligned} \frac{r_s}{r_s^0} &= 1 + 2I\left(\frac{\omega}{c}\right) \cos \theta_i d_{\parallel} + \dots \\ \frac{r_p}{r_p^0} &= 1 + 2I\left(\frac{\omega}{c}\right) \cos \theta_i \left[d_{\parallel} - \frac{\epsilon}{\epsilon \cot^2 \theta_i - 1} (d_{\perp} - d_{\parallel}) \right] + \dots \end{aligned} \quad (9)$$

where θ_i is the angle of incidence, r^0 is the reflectivity of the bare interface, ϵ is the relative dielectric constant of the substrate, and the d parameters are defined in terms of the normalized excess interface polarization.⁸⁰

From eq 9, it is straightforward to show that the ellipsometric variables Ψ and Δ are related to the difference in the d parameters

$$\tan \Psi e^{i\Delta} \equiv \frac{r_p}{r_s} = \frac{r_p^0}{r_s^0} \left[1 - 2I \frac{\omega}{c} \cos \theta_i \frac{\epsilon}{\epsilon \cot^2 \theta_i - 1} (d_{\perp} - d_{\parallel}) + \dots \right] \quad (10)$$

For a molecular film characterized by a thickness w and uniaxial dielectric function ϵ , the d parameters are⁷⁹

$$\begin{aligned} d_{\parallel} &= -w \frac{\epsilon_{xx} - 1}{\epsilon - 1} \\ d_{\perp} &= -w \frac{1/\epsilon_{zz} - 1}{1/\epsilon - 1} \end{aligned} \quad (11)$$

whereas if the film is treated as a layer of polarizable molecules

with surface density N ,

$$\begin{aligned} d_{\parallel} &= -\frac{4\pi N}{1 - \epsilon} \gamma_{xx} \\ d_{\perp} &= -\frac{4\pi N}{1 - \epsilon} \gamma_{zz} \end{aligned} \quad (12)$$

where γ is the effective volume polarizability ($\gamma \equiv$ polarizability/ $(4\pi\epsilon_0)$) tensor of the molecule, defined in terms of the electric field in the absence of the layer E^0 ,

$$\begin{aligned} p_z &= 4\pi\epsilon_0 \gamma_{zz} E_z^0 \\ p_x &= 4\pi\epsilon_0 \gamma_{xx} E_x^0 \end{aligned} \quad (13)$$

where p is the surface averaged dipole per molecule. γ includes all local field and molecular coupling effects. γ is related to the surface susceptibility tensor defined by Servant and Dignam⁸¹ by $\gamma = \gamma_{\text{servant}}/(4\pi N)$. From eqs 10 and 12, one can see that SE is sensitive to the weighted polarizability difference.

$$\begin{aligned} -\left[\frac{r_p}{r_s} \frac{r_s^0}{r_p^0} - 1 \right] &\sim \frac{\omega}{c} \frac{2I \cos \theta_i}{\cot^2 \theta_i - 1/\epsilon} \frac{N4\pi}{1 - \epsilon} (\epsilon\gamma_{zz} - \gamma_{xx}) \\ &\sim \frac{(\epsilon\gamma_{zz} - \gamma_{xx})}{S} \end{aligned} \quad (14)$$

For completeness, we note that eqs 11 and 12 can be combined to give the effective dielectric function of a molecular film in terms of γ .

$$\begin{aligned} \epsilon_{xx} - 1 &= 4\pi \frac{N}{w} \gamma_{xx} \\ \frac{\epsilon_{zz} - 1}{\epsilon_{zz}} &= 4\pi \frac{N}{w} \gamma_{zz} \end{aligned} \quad (15)$$

For a bulk sample, the dielectric constant is related to the volume polarizability α via the local field correction f as

$$\frac{\epsilon - 1}{1 + f(\epsilon - 1)} = 4\pi\rho\alpha \quad (16)$$

For an isotropic material, the Lorentz local field correction is $f = 1/3$. Equation 15 can be recognized as relating ϵ to γ via the local field corrections appropriate to an oblate ellipsoid (pancake), $f_z = 1$, $f_x = 0$.⁸²

References and Notes

- (1) Tour, J. M.; Jones, L., II; Pearson, D. L.; Lamba, J. J. S.; Burgin, T. P.; Whitesides, G. M.; Allara, D. L.; Parikh, A. N.; Atre, S. V. *J. Am. Chem. Soc.* **1995**, *117*, 9529–9534.
- (2) Allara, D. L.; Dunbar, T. D.; Weiss, P. S.; Bumm, L. A.; Cygan, M. T.; Tour, J. M.; Reinerth, W. A.; Yao, Y.; Kozaki, M.; Jones, L. *Molecular Electronics: Science and Technology*; Aviram, A., Ratner, M., Eds.; Annals of the New York Academy of Science 852; New York Academy of Science: New York, 1998; pp 349–370.
- (3) Tour, J. M. *Acc. Chem. Res.* **2000**, *33*, 791–804.
- (4) Adams, D. M.; Brus, L.; Chidsey, C. E. D.; Creager, S.; Creutz, C.; Kagan, C. R.; Kamat, P. V.; Lieberman, M.; Lindsay, S.; Marcus, R. A.; Metzger, R. M.; Michel-Beyerle, M. E.; Miller, J. R.; Newton, M. D.; Rolison, D. R.; Sankey, O.; Schanze, K. S.; Yardley, J.; Zhu, X. Y., *J. Phys. Chem. B* **2003**, *107*, 6668–6697.
- (5) Chen, J.; Reed, M. A.; Rawlett, A. M.; Tour, J. M. *Science* **1999**, *286*, 1550–1552.

- (6) Chen, J.; Wang, W.; Reed, M. A.; Rawlett, A. M.; Price, D. W.; Tour, J. M. *Appl. Phys. Lett.* **2000**, *77*, 1224–1226.
- (7) Dhirani, A.; Lin, P.-H.; Guyot-Sionnest, P.; Zehner, R. W.; Sita, L. R. *J. Chem. Phys.* **1997**, *106*, 5249–5253.
- (8) Fan, F.-R. F.; Yang, J. P.; Cai, L. T.; Price, D. W.; Dirk, S. M.; Kosynkin, D. V.; Yao, Y. X.; Rawlett, A. M.; Tour, J. M.; Bard, A. J. *J. Am. Chem. Soc.* **2002**, *124*, 5550–5560.
- (9) Ramachandran, G. K.; Hopson, T. J.; Rawlett, A. M.; Nagahara, L. A.; Primak, A.; Lindsay, S. M. *Science* **2003**, *300*, 1413–1416.
- (10) Donhauser, Z. J.; Mantooth, B. A.; Kelly, K. F.; Bumm, L. A.; Monnell, J. D.; Stapelton, J. J.; Price, D. W., Jr.; Rawlett, A. M.; Allara, D. L.; Tour, J. M.; Weiss, P. A. *Science* **2001**, *292*, 2303–2306.
- (11) Creager, S.; Yu, C. G.; Bamdad, C.; O'Connor, S.; MacLean, T.; Lam, E.; Chong, Y.; Olsen, G. T.; Luo, J. Y.; Gozin, M.; Kayyem, J. F. *J. Am. Chem. Soc.* **1999**, *121*, 1059–1064.
- (12) Dhirani, A.; Zehner, R. W.; Hsung, R. P.; Guyot-Sionnest, P.; Sita, L. R. *J. Am. Chem. Soc.* **1996**, *118*, 33190–3320.
- (13) Zehner, R. W.; Sita, L. R. *Langmuir* **1997**, *13*, 2973–2979.
- (14) Lin, P.-H.; Guyot-Sionnest, P. *Langmuir* **1999**, *15*, 6825–6828.
- (15) Cai, L.; Yao, Y.; Yang, J.; Price, D. W., Jr.; Tour, J. M. *Chem. Mater.* **2002**, *14*, 2905–2909.
- (16) Yang, G.; Qian, Y.; Engrakul, C.; Sita, L. R.; Liu, G.-Y. *J. Phys. Chem. B* **2000**, *104*, 9059–9062.
- (17) Bumm, L. A.; Arnold, J. J.; Cygan, M. T.; Dunbar, T. D.; Burgin, T. P.; Jones, L., II; Allara, D. L.; Tour, J. M.; Weiss, P. S. *Science* **1996**, *271*, 1705–1707.
- (18) Kushmeric, J. G.; Holt, D. B.; Yang, J. C.; Naciri, J.; Moore, M. H.; Shashidhar, R. *Phys. Rev. Lett.* **2002**, *89*, 086802.
- (19) Rawlett, A. M.; Hopson, T. J.; Nagahara, L. A.; Tsui, R. K.; Ramachandran, G. K.; Lindsay, S. M. *Appl. Phys. Lett.* **2002**, *81*, 3043–3045.
- (20) Dunbar, T. D.; Cygan, M. T.; Bumm, L. A.; McCarty, G. S.; Burgin, T. P.; Reinerth, W. A.; Jones, L.; Jackiw, J. J.; Tour, J. M.; Weiss, P. S.; Allara, D. L. *J. Phys. Chem. B* **2000**, *104*, 4880–4893.
- (21) Stapleton, J. J.; Harder, P.; Daniel, T. A.; Reinard, M. D.; Yao, Y.; Price, D. W.; Tour, J. M.; Allara, D. L. *Langmuir* **2003**, *19*, 8245–8255.
- (22) Seminario, J. M.; Zacarias, A. G.; Tour, J. M. *J. Am. Chem. Soc.* **2000**, *122*, 3015–3020.
- (23) Karzazi, Y.; Cornil, J.; Bredas, J. L. *Nanotechnology* **2003**, *14*, 165–171.
- (24) Gonzalez, C.; Mujica, V.; Ratner, M. A. *Ann. N. Y. Acad. Sci.* **2002**, *960*, 163–176.
- (25) Richter, L. J.; Petralli-Mallow, T. P.; Stephenson, J. C. *Opt. Lett.* **1998**, *23*, 1594.
- (26) S polarization is defined as having an electric vector perpendicular to both the incident wavevector \mathbf{k} and the outward surface normal \mathbf{n} , whereas P polarization is defined as $S \times \mathbf{k}$ and lies in the plane of incidence.
- (27) We identify certain commercial equipment, instruments, or materials in this article to specify adequately the experimental procedure. In no case does such identification imply recommendation or endorsement by the National Institute of Standards and Technology, nor does it imply that the materials or equipment identified are necessarily the best available for the purpose.
- (28) Varsanyi, G. *Vibrational Spectra of Benzene Derivatives*; Academic Press: New York, 1969.
- (29) Displacement vectors for the modes in Tables 2 and 3 are provided in the Supporting Information.
- (30) Chen, Z.; Shen, Y. R.; Somorjai, G. A. *Annu. Rev. Phys. Chem.* **2002**, *53*, 437–465.
- (31) Buck, M.; Himmelhaus, M. *J. Vac. Sci. Technol. A* **2001**, *19*, 2712–2736.
- (32) Richmond, G. L. *Annu. Rev. Phys. Chem.* **2001**, *52*, 357–389.
- (33) Miranda, P. B.; Shen, Y. R. *J. Phys. Chem. B* **1999**, *103*, 3292–3307.
- (34) Bain, C. D. *J. Chem. Soc., Faraday Trans.* **1995**, *91*, 1281.
- (35) Shen, Y. R. *Nature* **1989**, *337*, 519–525.
- (36) Gautam, K. S.; Schwab, A. D.; Dhinojwala, A. *Phys. Rev. Lett.* **2000**, *85*, 3854–3857.
- (37) Gautam, K. S.; Schwab, A. D.; Dhinojwala, A. *Macromolecules* **2001**, *34*, 1137–1139.
- (38) Hirose, C.; Yamamoto, H.; Akamatsu, N.; Domen, K. *J. Phys. Chem.* **1993**, *97*, 10064–10069.
- (39) Zhang, D.; Gutow, J.; Eisenthal, K. B. *J. Phys. Chem.* **1994**, *98*, 13729–13734.
- (40) Zhuang, X.; Miranda, P. B.; Kim, D.; Shen, Y. R. *Phys. Rev. B* **1999**, *59*, 12632–12640.
- (41) Hirose, C.; Akamatsu, N.; Domen, K. *J. Chem. Phys.* **1992**, *96*, 997.
- (42) Duffy, D. C.; Davies, P. B.; Bain, C. D. *J. Phys. Chem.* **1995**, *99*, 15241–15246.
- (43) Wei, X.; Hong, S.-C.; Zhuang, X.; Goto, T.; Shen, Y. R. *Phys. Rev. E* **2000**, *62*, 5160–5172.
- (44) Becke, A. D. *J. Chem. Phys.* **1993**, *98*, 1372–1377.
- (45) Lee, C.; Yang, W.; Parr, R. G. *Phys. Rev. B* **1988**, *37*, 785–789.
- (46) *Gaussian 98, Revision A.9*. Frisch, M. J.; Trucks, G. W.; Schlegel, H. B.; Scuseria, G. E.; Robb, M. A.; Cheeseman, J. R.; Zakrzewski, V. G.; Montgomery, J. A., Jr.; Stratmann, R. E.; Burant, J. C.; Dapprich, S.; Millam, J. M.; Daniels, A. D.; Kudin, K. N. O.; Strain, F. M. C.; Farkas, O.; Tomasi, J.; Barone, V.; Cossi, M.; Cammi, R.; Mennucci, B.; Pomelli, C.; Adamo, C.; Clifford, S.; Ochterski, J.; Petersson, G. A.; Ayala, P. Y.; Cui, Q.; Morokuma, K.; Malick, D. K.; Rabuck, A. D.; Raghavachari, K.; Foresman, J. B.; Cioslowski, J.; Ortiz, J. V.; Baboul, A. G.; Stefanov, B. B.; Liu, G.; Liashenko, A.; Piskorz, P.; Komaromi, I.; Gomperts, R.; Martin, R. L.; Fox, D. J.; Keith, T.; Al-Laham, M. A.; Peng, C. Y.; Nanayakkara, A.; Challacombe, M.; Gill, P. M. W.; Johnson, B.; Chen, W.; Wong, M. W.; Andres, J. L.; Gonzalez, C.; Head-Gordon, M.; Replogle, E. S.; Pople, J. A. Gaussian Inc.: Pittsburgh, PA, 1998.
- (47) The Raman polarizability derivative is symmetric within the approximations employed in Gaussian 98.
- (48) Eisert, F.; Dannenberger, O.; Buck, M. *Phys. Rev. B* **1998**, *58*, 10860–10870.
- (49) Uncertainties are 1 SD on the basis of the diagonal elements of the error matrix.
- (50) In spectroscopic ellipsometry, the complex ratio of the electric field reflectivity factors for s- and p-polarized light ρ is measured and reported in terms of angles ψ and Δ : $r = (r_p/r_s) = \tan \psi \exp[i\Delta]$.
- (51) The values $n \approx 1.50$ and $t \approx 2.3$ nm are consistent with J. Shi et al., ref 52.
- (52) Shi, J.; Hong, B.; Parikh, A. N.; Collins, R. W.; Allara, D. L. *Chem. Phys. Lett.* **1995**, *246*, 90–94.
- (53) Casson, B. D.; Bain, C. D. *Langmuir* **1997**, *13*, 5465–5469.
- (54) Losurdo, M.; Giangregorio, M. M.; Capezzuto, P.; Bruno, G. V.; Baburdi, F.; Colangiuli, D.; Farinols, G. M.; Francesco, N. *Macromolecules* **2003**, *36*, 4492–4497.
- (55) Tammer, M.; Monkman, A. P. *Adv. Mater.* **2002**, *14*, 210–211.
- (56) Martin, S. J.; Godschalx, J. P.; Mills, M. E.; Shaffer, E. O., II; Townsend, P. H. *Adv. Mater.* **2000**, *12*, 1769–1778.
- (57) Reported error bars are 1 σ averaged over the three independent sample sets.
- (58) Hyperchem, Inc., 115 North West 4th St., Gainesville, FL 32601.
- (59) Feibelman, P. J. *Prog. Surf. Sci.* **1982**, *12*, 287.
- (60) Feibelman, P. J. *Phys. Rev. B* **1981**, *23*, 2629.
- (61) Liebsch A. *Electronic Excitations at Metal Surfaces*; Plenum: New York, 1997.
- (62) Azzam, R. M. A.; Bashara, N. M. *Ellipsometry and Polarized Light*; North-Holland: Amsterdam, 1977.
- (63) Bell, G. R.; Li, Z. X.; Bain, C. D.; Fischer, P.; Duffy, D. C. *J. Phys. Chem. B* **1998**, *102*, 9461–9472.
- (64) Wilson, P. T.; Richter, L. J.; Wallace, W. E.; Briggman, K. A.; Stephenson, J. C. *Chem. Phys. Lett.* **2002**, *363*, 161–168.
- (65) Humbert, C.; Muck, M.; Claderone, A.; Vigneron, J.-P.; Meunire, V.; Champagne, B.; Zheng, W. Q.; Tadjeddine, A.; Thiry, P. A.; Peremans, A. *Phys. Status Solidi* **1999**, *175*, 129–136.
- (66) Wan, L. J.; Terashima, M.; Noda, H.; Osawa, M. *J. Phys. Chem. B* **2000**, *104*, 3563–3569.
- (67) In Table 3 of Appendix I, there is an error in the correction applied to the nitro modes to account for the transition dipole orientation. If the transition dipole orientation calculated in our work is used to analyze the IR data of I, an orientation for the nitro-OPE of $\theta = 33^\circ \pm 9^\circ$ and $\psi 65^\circ \pm 30^\circ$ is obtained.
- (68) Simpson, G. J.; Rowlen, K. L. *Acc. Chem. Res.* **2000**, *33*, 781–789.
- (69) Jelly, E. E. *Nature* **1937**, *139* 631. Scheibe, G. *Angew. Chem.* **1936**, *49*, 563. Norland, K.; Ames, A.; Taylor, R. *Photogr. Schi. Eng.* **1970**, *14*, 295.
- (70) Yassar, A.; Horowitz, G.; Valat, P.; Wintgens, V.; Hmyene, M.; Deloffre, F.; Srivastava, P.; Lang, P.; Garnier, F. *J. Phys. Chem.* **1995**, *99*, 9155–9159.
- (71) McRae, E. G.; Kasha, M. *Physical Processes in Radiation Biology*; Augenstein, L. G., Mason, R., Rosenberg, B., Eds.; Academic Press: New York, 1964, pp 23–42.
- (72) Hochstrasser, R. M.; Kasha, M. *Photochem. Photobiol.* **1964**, *3*, 317–331.
- (73) $M^2 = 1.02 \times 10^{-61} \nu \epsilon \text{ dv}$, MCm, $\nu \text{ cm}^{-1}$, $\epsilon \text{ dm}^3 \text{ mol}^{-1} \text{ cm}^{-1}$.
- (74) Shen, Y. R. *Appl. Phys. B* **1999**, *68*, 295 and references therein.
- (75) Guyot-Sionnest, P.; Chen, W.; Shen, Y. R. *Phys. Rev. B* **33** **1986**, 8254–8263.
- (76) Sipe, J. E. *J. Opt. Soc. Am.* **1987**, *B4*, 481.
- (77) Butcher, P. N.; Cotter, D. *The Elements of Nonlinear Optics*; Cambridge University Press: Cambridge, 1990; Chapter 4.

(78) Hirose, C.; Akamutsu, N.; Domen, K. *Appl. Spectrosc.* **1992**, *46*, 1051–1072.

(79) Chen, W.; Schaich, W. L. *Surf. Sci.* **1989**, *218*, 580–602 and references therein.

(80) Schaich, W. L.; Chen, W. *Phys. Rev. B* **1989**, *39*, 10714–10724.

(81) Servant, L.; Dignam, M. J. *Thin Solid Films* **1994**, *242*, 21–25.

(82) Feynman, R. P. *Lectures on Physics*; PUBLISHER AND CITY???, 1970.